

Long-slit cross-dispersion spectroscopy for Hyperion UV space telescope

Heejoo Choi,^{a,b} Isaac Trumper,^{a,c} Yi-Ting Feng^{✉,a}, Hyukmo Kang^{✉,a},
Joel Berkson,^a Haeun Chung^{✉,d}, Erika Hamden^{✉,d},
and Dae Wook Kim^{a,b,d,*}

^aUniversity of Arizona, Wyant College of Optical Sciences, Tucson, Arizona, United States

^bUniversity of Arizona, Large Binocular Telescope Observatory, Tucson, Arizona, United States

^cELE Optics, Inc., Tucson, Arizona, United States

^dUniversity of Arizona, Department of Astronomy and Steward Observatory, Tucson,
Arizona, United States

Abstract. Molecular clouds are a crucial stage in the lifecycle of a star, and the far ultraviolet (FUV) spectral range is a prime observation band. Hyperion is an FUV space telescope that investigates the birth clouds of stars using a high-resolution spectrometer. To meet the scientific requirements, we developed and evaluated a spectrometer that covers the 140.5 to 164.5 nm wavelength range with a spectral resolution higher than 30,000. We employed on-axis and on-plane dispersive optic layouts to control the aberration from a large aspect ratio slit (10 arcmin \times 2.5 arcsec, aspect ratio $R = 240$). The cross-dispersion isolates three orders from the échelle grating ($n = -19, -18,$ and -17), and the subsequent two-mirror freeform imaging optics form a two-dimensional spectral distribution on a 50 mm \times 50 mm detector array. The geometrical and spectral performances of this innovative design are evaluated. © 2021 Society of Photo-Optical Instrumentation Engineers (SPIE) [DOI: [10.1117/1.JATIS.7.1.014006](https://doi.org/10.1117/1.JATIS.7.1.014006)]

Keywords: space telescope; far-UV spectroscopy; Échelle grating; freeform optic.

Paper 20133 received Sep. 1, 2020; accepted for publication Feb. 26, 2021; published online Mar. 12, 2021.

1 Introduction

During the very first stage of star formation (SF), molecules, atoms, and ionizing ultraviolet light permeate dynamic and dense regions of space. Collapsing cores, created by instabilities triggered by shocks and turbulence, slowly condense. As new stars are born, their intense ultraviolet (UV) radiation carves holes into their nascent molecular cloud, typically within the first 1 megayear (Myr).¹ Molecular hydrogen (H₂) is the most abundant molecule and is central to the process of SF. Understanding the role molecular clouds play in the lifecycle of stars and galaxies is critical for all fields of astronomy.^{2,3} We can determine the rate at which stars formed in the past,^{4,5} but we lack the fundamental knowledge to predict when and where SF will occur next, even in our galaxy.³

The primary scientific goal of the UV space telescope Hyperion (Fig. 1) is to examine the fuel for SF by probing the nature, extent, and state of H₂ at the crucial atomic-to-molecular interstellar medium boundary layer. The telescope apparatus must observe from above Earth's UV-blocking atmosphere because the target spectral band (UV-H₂) is only accessible from space. It will observe the precise location where molecular clouds meet their surrounding environment, elucidating their evolutionary history, present state, and possible futures. Because the targeted H₂ fluorescences are intrinsically very narrow and there are many closely spaced lines depending on the excitation level, high-resolution spectroscopy (e.g., $R > 30,000$) is essential for this mission. The Hyperion mission also targets spectral broadening due to 10 km range thermal/turbulent motion. These measured physical parameters uncover the relationship between SF, cloud evaporation in the presence of a radiation field, and how a forming star itself impacts SF efficiency

*Address all correspondence to Dae Wook Kim, dkim@optics.arizona.edu



Fig. 1 3-D rendered image of the UV space telescope Hyperion examining the fuel for SF by probing the nature, extent, and state of H_2 at the crucial atomic-to-molecular interstellar medium boundary layer.

across galactic star-forming regions. Hyperion examines the fuel for SF directly by observing the molecular interface between dense, star-forming clouds, the diffuse interstellar environment, and the stars that arise from these regions by observation of H_2 in emission within range of 140.5 to 164.5 nm.

The optical performance requirement of the Hyperion mission is 5 arcsec spatial resolution, 10 arcmin instantaneous field of view (FOV), $R > 30,000$ spectral resolution (i.e., $\lambda/\Delta\lambda$), and photometric precision at 2%. To meet the optical requirements, we adopted δ -doped charge-coupled devices (CCDs)^{6–8} with a combination of an échelle grating, cross-dispersion, and a freeform optics imaging system.⁹ However, it is challenging to have low aberration of the long-slit image at the sensor plane for fast diffractive rays after the échelle grating and cross-dispersion. We solved this problem using a center hole in the échelle grating to allow an on-axis layout with no photon loss. Moreover, careful selection of the collimating and downstream optics confined the small spot at the sensor to have the $R > 30,000$ with reasonable throughput.

Spectroscopy in space environment adds complexity to the optical design because of the requirement of the science-driven specification and the limited volume assigned to the payload. The pioneer of modern far ultraviolet (FUV) missions is the International Ultraviolet Explorer (IUE) by NASA, UK Science Research Council, and European Space Agency in 1978. It was designed to aim a high-resolution spectra observation and has had highly successful accomplishments.^{10,11} Also, as an add-on equipment of the Hubble Space Telescope (HST), STIS (Space Telescope Imaging Spectrograph, mission STS-82, 1997),^{12,13} and COS (Cosmic Origins Spectrograph, mission STS-125, 2009)¹⁴ have been successfully installed into HST and served versatile UV spectrograph observations. These spectroscopy instruments have adopted various flat, parabolic, and/or échelle gratings with slits.

Regarding Medium-Class Explorers (MIDEX) and Small-Class Explorers (SMEX) mission, in the last couple of decades, researchers, and scientists have launched several space-based UV telescopes, with Galaxy Evolution Explorer (GALEX, SMEX)^{15–17} and far ultraviolet Spectroscopic Explorer (FUSE, MIDEX)^{18,19} as outstanding representative missions. Even though both operated in the FUV, the dispersive methods are different. GALEX utilized a dichroic beam splitter combined with grism, and FUSE used a four-segmented Rowland circle layout that has been adopted for spacecraft spectroscopy.^{20–22} The simple optical arrangement and low spectral aberration are attractive advantages of the Rowland design for a compact and low-cost instrument. As long as the detectors can be installed at the curved Rowland circle, and a relatively narrow spectral range is required, the Rowland is a good solution. Multiple sets of cascaded Rowland spectrographs can be adopted to cover broad spectrums.²³ Table 1 shows a comparison of the key specifications between some previous UV space missions and Hyperion.

However, contemporary astrophysics pushes the optical performance to the limit, and Hyperion's optical design required creative solutions. The desired spectral resolution imaging quality cannot be achieved by traditional cross-dispersion spectroscopy design methods such as a grating combined with a prism due to the limited overall volume constraints of the Hyperion spectrograph. Also, the low transmission efficiency (i.e., high absorption) of prisms is another

Table 1 Comparison of key performance parameters of UV observing mission benchmarks and Hyperion.

Parameters	GALEX	FUSE	Hyperion
Spectral range (Å)	FUV: 1344 to 1786 NUV: 1771 to 2831	905 to 1187	1405 to 1645
Spectral resolution R ($\lambda/\Delta\lambda$)	FUV: 200 NUV: 90	2400 to 30,000	>30,000
Dispersive type	Dichroic beam splitter + grism	Rowland circle, four sets of gratings, and two sets of sensors	Échelle + cross-dispersion
Optics coating/mirror	MgF ₂ /Al	SiC/Al (905 to 1103 Å) LiF/Al (980 to 1187 Å)	MgF ₂ /Al
Slit aperture size	4.3 in. (no slit, image resolution)	1.25 in × 20 in, 4 in × 20 in., 30 in. × 30 in.	2.5 in. × 10 in.
Telescope type (primary mirror diameter)	Ritchey-Chretien (50 cm)	4 OAPs (4 × 38.7 × 35.2 cm)	Ritchey-Chretien (40 cm)

reason to eliminate the use of a prism. We present an enabling design solution using a cross-dispersion and freeform mirrors in a compact folded path configuration.⁹

This paper is organized as follows: In Sec. 2, we describe the optical design boundary for science. In Sec. 3, we detail the optical design to perform the required specification, and the geometric and spectrometric performance evaluations are presented in Sec. 4.

2 Optical Design Boundary Conditions and Challenges

2.1 High-Dynamic-Range δ -Doped CCD Sensor

The science mission of Hyperion depends on the performance of the instrument and available technology. The detector array of the telescope defines the measurable spectral range due to the bandgap of the doped materials in semiconductors, which limits the space mission's measurable objects. Hyperion's target is a FUV spectrum, but the usual Si-based detector array will not see this spectrum. It is worth to note that, for various FUV applications, the microchannel plate (MCP) has been utilized with various benefits (e.g., solar blind photocathodes with ~20% quantum efficiency (QE), windowless operation in vacuum, low dark counts). Recently developed borosilicate MCPs show a greatly improved dynamic range, also.²⁴

These quantum efficient challenges have been overcome thanks to NASA technology developments.^{6–8} The δ -doped CCDs (Fig. 2), developed by JPL (Jet Propulsion Laboratory) scientists, allow the high-resolution emission measurement of UV-H₂. The δ -doped CCDs have good efficiency in the UV, with the application of specialized antireflection coatings. The Hyperion design uses a simple MgF₂ coating to achieve >55% QE in the bandpass. This number exceed the MCP QE of the successful previous FUV mission such as GALEX (10% to 15%) and HST/COS (20% to 25%) at Hyperion target band.⁷ The higher dynamic range of a CCD means that we have the ability to measure from bright to dim objects without enlarge primary mirror. In addition, the fabrication and operation of the δ -doped CCDs are more relaxed and inexpensive than MCP with respect to prices and power requirements. The specifications of the δ -doped CCD detector are summarized in Table 2.

2.2 High Spectral Resolution Instrument in Compact Form Factor

A conventional spectroscopic design uses a point source input (or slit) that is imaged on to the sensor plane, or the exit slit, with close to unity magnification. Basically, the series of optics in

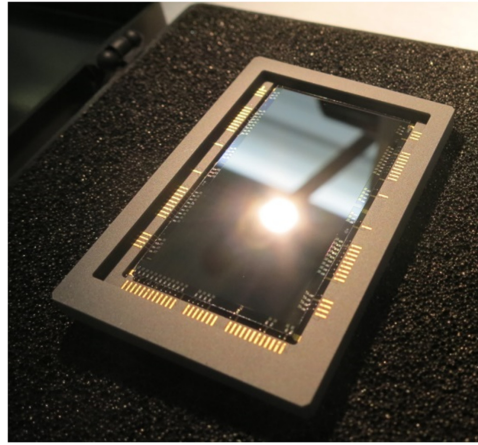


Fig. 2 The δ -doped CCD, developed by JPL scientists, allows for high-resolution emission measurement of UV-H₂, and is used as the scientific camera focal plane array for the Hyperion space telescope design (Photo credit to Todd Jones, JPL). The sensor in the photo is a rectangular format prototype and the full-size square format sensor (49 × 49 mm) for Hyperion will be manufactured.

Table 2 δ -doped CCD specification defining the Hyperion focal plane array.

Parameter	Specification
δ -doped CCD detector efficiency	QE > 50% in band
Array size	4096 × 4096 pixels
Detector size	49.152 × 49.152 mm
Pixel pitch	12 μ m
Serial readout frequency	140 kHz
FPA readout time (quad outputs)	30 s
Power dissipation in CCD	0.15 W (integrate/standby)
FPS read noise	4 e-
Detector temperature	< -80°C ± 0.1°C
Mean dark signal	-80°C 0.0019 e-/pix/s
Digitization	14 bits/p

the spectrograph (except the grating) endeavors to narrow the image of the small input beam as much as possible on the sensor plane. To accomplish this, three primary groups of optical components are used: collimation, dispersion, and imaging optics. A ruled diffraction grating is commonly used as the dispersive element, and sometimes its base surface has a curvature to combine it with the collimation group. Collimating the light from the input slit to the grating is relatively easy compared to imaging because the inserted beam is usually close to a point source or only a single dimension FOV (slit), which can be collimated without significant field aberrations by means of a concave mirror (e.g., off-axis parabolic mirror). After the light interacts with the grating, the light is dispersed into a wide range of angles as it is diffracted. The imaging optics group needs to accommodate this large chromatic FOV while maintaining good image quality. Distortion of the slit presents one of the many challenges in producing a high spectral resolution $R = \lambda/\Delta\lambda$.²⁵

In general, possible methods to increase the spectral resolution include increasing the distance after the grating, wide diffraction from the grating (higher groove density or higher diffraction order), and high-resolution imaging systems and sensors. The long propagation of the beam requires a large volume for the spectrometer, and therefore it is not a preferred solution for a space mission where instrument volume and mass are driving requirements. The beams from a fast-dispersive grating are spread in a broad angle after the grating, which means that the imaging optics design will encounter a more extensive chromatic field acceptance. Finally, the pixel pitch of the sensor is defined by the semiconductor manufacturing process. A better imaging system for small spots on the sensor, and a wide FOV for a diffractive beam after the grating, would be a promising solution for a high-resolution spectrometer.

3 Échelle and Freeform Optical Design for Hyperion

3.1 Overall Optical Layout of the Échelle Cross-Dispersion Spectrometer

Hyperion has adopted a significantly longer slit length than FUSE for spatial FOV. The extreme aspect ratio of the long-slit ($10 \text{ arcmin} \times 2.5 \text{ arcsec}$, aspect ratio of 240) and the very high spectral resolution requirement ($R > 30000$) at the FUV spectral range (1405 to 1645 Å) make the optical design of Hyperion unique by utilizing the freeform and cross-dispersion configuration design approach. In order to achieve this high spectral resolution exceeding the limit of traditional spectrograph's off-axis optics layout, we applied a nontraditional design with the illumination of the collimating mirror on-axis through the center hole of the échelle grating and the incorporation of freeform imaging optics (Fig. 3).⁹ It is important to acknowledge that the cross-dispersion with two consecutive gratings and the selection of high diffraction orders have been used for Keck HIRES (High Resolution Échelle Spectrometer).²⁶

Because our target FOV is relatively wide (10 arcmin, slit length direction), the Ritchey-Chrétien telescope design (i.e., hyperbolic mirror for primary and secondary) is adopted. After the telescope, the $F/6$ (effective focal length EFL = 2400 mm) beam enters the spectrometer instrument.

The telescope first passes the beam to the on-axis échelle grating. In traditional spectrometer design, the planar grating is placed off-axis from the inserted ray optic axis. However, the slanted long-slit beam entering the fast dispersive échelle grating (−17th to −19th orders) induces significant aberration (e.g., astigmatism and coma aberration along the slit).

We resolved the aberration issue by cutting out the hole at the center of the échelle grating and placing the slit on-axis of the telescope to create a normal incidence angle to the échelle grating, as shown in Fig. 4(b). Because of the annular pupil of the Ritchey-Chrétien, caused

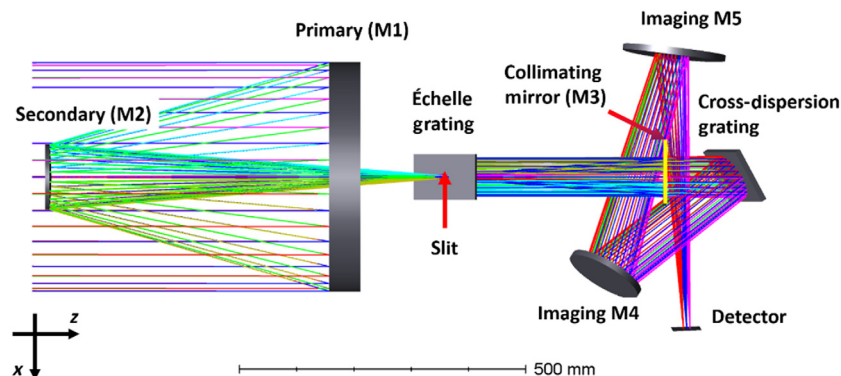


Fig. 3 The overall layout of the long-slit cross-dispersion échelle freeform spectroscopy for the Hyperion UV space telescope. The $F/6$ beam from the Ritchey-Chrétien goes into the long slit. The slit is uniquely placed at the échelle grating center hole. The central hole of the échelle grating enables the collimator and échelle grating to be placed on-axis to minimize the aberration.⁹

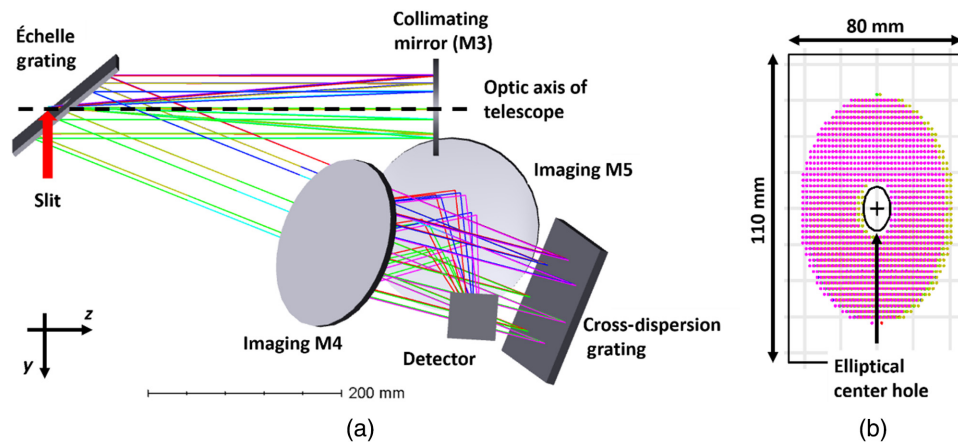


Fig. 4 (a) Optical layout of the spectrometer instrument and footprint diagram (pupil image) of all fields on the first échelle grating. The diffraction angle of the échelle and cross-dispersion are orthogonal to each other. (b) Annular type échelle grating with a central hole (matching the secondary mirror obscuration) allows the unique on-axis optical layout without photon loss.⁹

by the secondary obstacle, the center hole approach does not induce any further photon loss. The long-slit is placed slightly behind the échelle grating to allow sufficient room for a wheel mount and motors.

The diffractive angle of the target spectral range (1405 to 1645 Å) on both grating surfaces are 5 deg at the first échelle grating and 3.8 deg at the second cross-dispersion grating. The freeform imaging optics should make spots on the 50 mm × 50 mm δ -doped CCD sensor from the ~ 104 mm × 68 mm ellipse pupil, and divergences of 5 deg and 3.8 deg from the two different conjugate planes. The broadening spot on the sensor means not only the loss of spatial but also spectral resolution.

3.2 Compact Type-4 Freeform Imaging Optics Layout

To accommodate a large cross-dispersed FOV while maintaining a small, focused spot, a freeform two-mirror imaging system (M4 and M5) was designed and optimized as an actual design application of the previously reported type-4 design form approach.²⁷ Rotationally, symmetric systems were not feasible in this instrument because of the constraint on volume. The two-mirror system employs a type-4 design form, which supports a large FOV in a compact volume, a critical factor for space missions.

Although a three-mirror design would provide better imaging performance,^{28,29} this would come at the expense of a larger volume requirement, as well as photon loss from the extra-reflector, leading to the choice of the two-mirror design. Furthermore, the use of the échelle grating on-axis means that all the dispersive elements (collimator, échelle grating, and cross-dispersion grating) can be placed along the same optical axis, reducing off-axis aberrations.^{30,31}

The two-mirror type-4 system can then have its folding direction along the same plane, leveraging the more straightforward aberration behavior for better optical performance. To accommodate the planar anamorphism at the échelle grating and rectangular field width of the slit, the collimator was specified with a biconic surface, which improves the pupil quality and reduces the aberration burden on the imaging system.

To couple the output from the diffractive optics, the entrance pupil of the imaging system must be placed at the échelle grating. The type-4 form supports a significant separation between its entrance pupil and the first mirror, easily accommodating the pupil matching requirement. The imaging optics in the type-4 layout are specified with standard Zernike polynomials (order up to the 50th term, presented in Table 4, Appendix A). The specific Hyperion design values are elucidated and summarized in Table 3 as a reference for those who want to benchmark or reproduce the design.

Table 3 Hyperion optical design values and component characteristics.

Parameters	Values
Telescope	
Primary mirror diameter (M1)	40 cm
Secondary mirror diameter (M2)	12.5 cm
<i>F</i> -number/EFL	6/240 cm
Spectrometer	
Wavelength range	140.5 to 164.5 nm
Entrance slit, FOV width	2.5 arcsec
Entrance slit, FOV height	10 arcmin
Slit width on detector	2.083 pixels
Wide slit (×2)	20 arcsec × 30 arcsec
Collimating optic (M3), biconic	$f_{lx} = 799$ mm Conic _x = −0.55 $f_{ly} = 800$ mm Conic _y = −1.4828
Échelle grating (EG), planar grating	
Aperture size	80 mm × 110 mm
α (incidence angle), β (diffractive angle), blaze angles	50 deg, 35 deg, 38.9 deg
Échelle grating groove density	450 lines/mm
Operating orders	$n = -19, -18, \text{ and } -17$
Cross dispersing grating	
Aperture size	100 mm × 150 mm
α, β , blaze angles	30 deg, 10 deg, 13.275 deg
Cross disperser groove density	2600 lines/mm
Operating order	$n = -1$
Imaging optics (M4 and M5)	
Primary imaging optic (M4)	Freeform (up to 50th term standard Zernike polynomials)
Secondary imaging optic (M5)	Freeform (up to 50th term standard Zernike polynomials)
Working <i>F</i> -number	8

4 Hyperion Optical Performance Analysis

4.1 Spectral and Spatial Resolution Performance

The image performance was evaluated with full-spectrum and full-field images. Six field points (four corners and two at the middle top and bottom) were defined to match the actual Hyperion slit size, as shown in Fig. 5.

The spot sizes for all fields and wavelengths are the first elements for optical performance evaluation. We selected the dispersion parameters (e.g., the groove and diffraction order, as listed

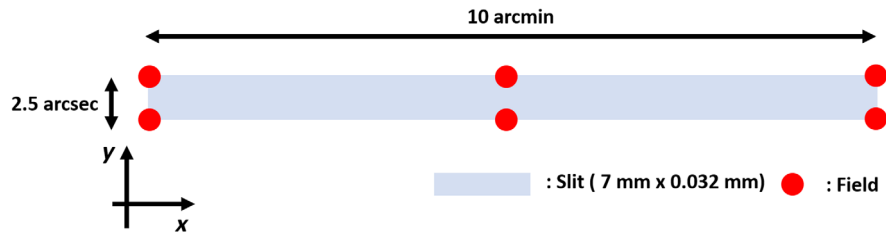


Fig. 5 The six defined field points and slit size according to the Hyperion's scientific target field requirement.

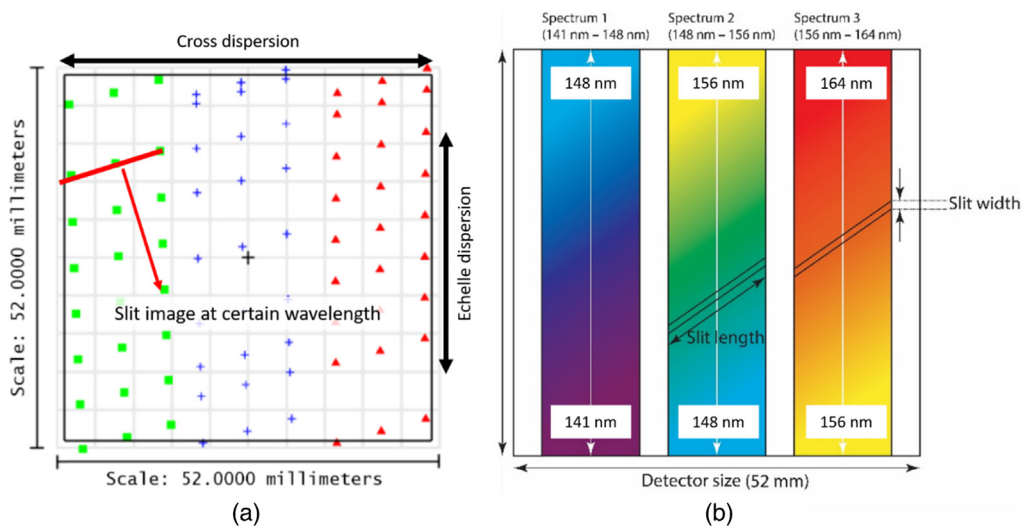


Fig. 6 (a) Footprint diagram of the full spectrum on the detector sensor plane⁹ and (b) the schematic diagrams of spectral distribution. The dispersion along the vertical is from the échelle grating, and the horizontal dispersion (three stripes) is from two consecutive cross-dispersion gratings. Due to the orientation of both grating and relay optics, the slit images are slightly tilted. Each field image on the sensor is confined in a small spot to meet $R > 30,000$.

in Table 3) of both gratings to cover the full spectrum within the given detector size in two-dimensional (2D) formation. The full cross-dispersed spectra are shown in Fig. 6.

Once well-defined spectral stripes were obtained on the sensor, the imaging optics were optimized to obtain a well-confined slit image of six fields. The blurred slit image induces the dispersed energy of a single wavelength, which overlaps with neighboring wavelengths. This overlap causes a loss of spectral resolution. To optimize the freeform imaging (M4 and M5) mirrors, the radii of curvature (and off-axis distance) for M4 and M5 were surveyed to set the initial layout for the following merit-function based numerical optimization.

During the optimization process high weight (in the figure of merit) was applied to the spot sizes at the center region of the sensor ($\lambda \sim 152$ nm) for all six fields in Fig. 5. When the spot sizes in the center region converged, the high order freeform Zernike terms (presented in Table 4, Appendix A) were set as variables and optimized to improve the spot sizes over the full wavelength range [i.e., the entire sensor area in Fig. 6(a)]. This is an effective approach because those noncenter region wavelength spots are equivalent to the off-axis field aberration control in a freeform imaging optical system optimization case. To achieve a small, well-defined spot over the 2D detector array, we balanced the need to create tight spot sizes at the edges of the spectral band (at the corners of the detector) with the need to optimize the fields near the center by adjusting the figure of merit weights between different wavelengths. After the iterative numerical optimization process, the final Hyperion design achieves the required $R > 30,000$, as shown in Fig. 7.

For the unique two-consecutive-grating design approach, each divergence occurs with a different angle at the various grating planes. By adopting the type-4 layout of the imaging optics, the wide anisotropic divergence angle from two different planes is well focused on the sensor.

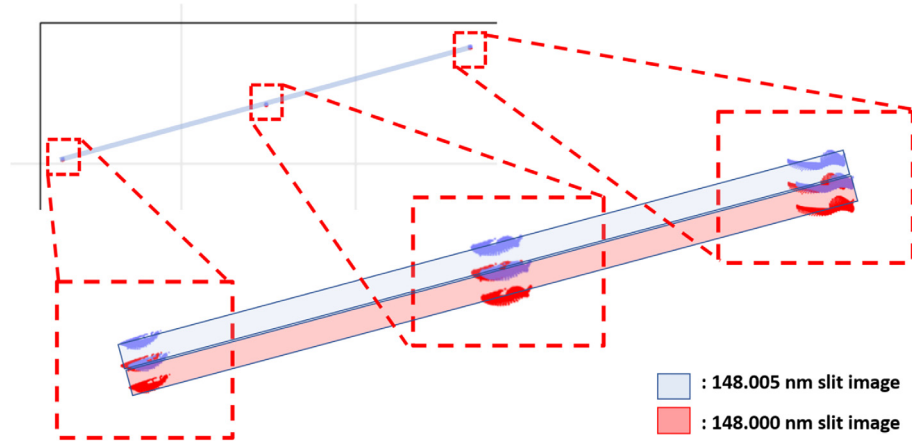


Fig. 7 Left top corner (of the detector) plane slit image ($\lambda = 148$ nm) and the smallest stepped neighboring wavelength. The inset images at each field are copied from magnified images in the simulation program. Six spots of the slit image simulate the four corners and middle of the slit. Even though the edge fields are overlapping, most of the energy is confined in the middle of slit.

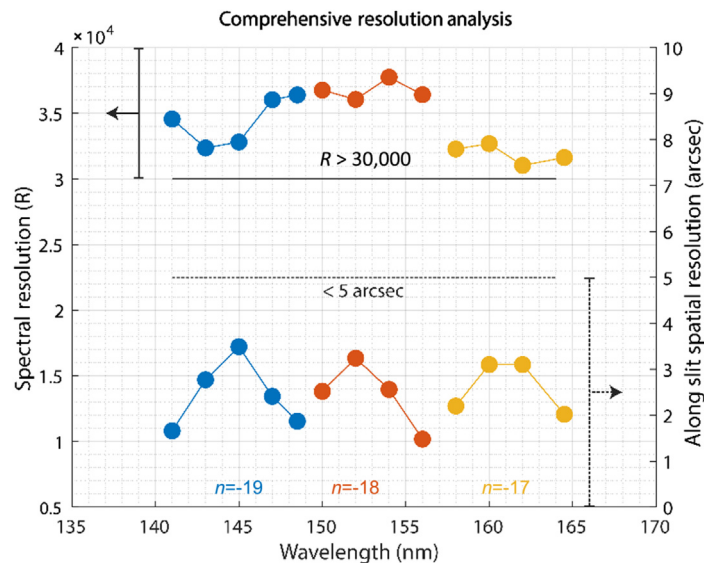


Fig. 8 Comprehensive resolution plot. The spectral and spatial scientific requirements are well satisfied.¹⁰

Because the prime purpose of this system is a high spectral resolution, a distinct minimum wavelength step is used to evaluate the resolution. The target spectral resolution is $R > 30,000$, corresponding to a spectral resolution of ~ 5 pm (picometer). To evaluate the spectral resolution of the system, we insert the target λ , and $\lambda + \Delta$ (5 pm), and analyze whether both slit images from those wavelengths are distinguishable (Fig. 7). The perimeter slit images also show equal quality over the detector array. The spatial resolution along the slit is < 5 arcsec for all fields and wavelengths, as the comprehensive resolution plot shows in Fig. 8.

4.2 Diffraction Efficiency Performance

A grating simulation using the sequential ray-tracing method has some limitations when calculating the entire range of diffractive properties. For instance, this approach uses the number of grooves on the grating, and its order, to calculate the diffractive angle, and these two variables are

the only available knobs to control the diffraction features. To evaluate all the physical phenomena of diffraction, the wave propagation approach is adequate for detailed grating simulation. The efficiency over the spectrum and corresponding blaze angles are fundamental inputs to evaluate the yield of FUV susceptibility and feasibility of the design. We used the RSoft (diffractMOD RCWA), together with the blaze angle, incidence angle, and diffraction order, to simulate the efficiency shown in Fig. 9.

The divergence angle of the spectrum is fast at high order, and this is beneficial for spectral resolution. However, as shown in Figs. 9(a)–9(c), the efficiency shows a rapidly declining trend over the spectrum. The chosen blaze angle focuses the energy in a certain direction, which causes a lack of photons for the perimeter spectrum of each order. We selected the blaze angle [38.9 deg, illustrated by the white vertical line in Figs. 9(a)–9(c)], while considering the incidence angle to the grating, so that the three orders have even efficiency. Because of the cross-dispersion approach, there is no issue with the overlapping in the free spectral range of the three orders where they have similar efficiency over the entire target spectrum range.

The essential role of the second grating is to isolate each band clearly. It uses a single diffraction order to separate overlapping stripes from the first échelle grating by leveraging a wide free spectral range. Moreover, the low order has flat efficiency for the entire spectral range with the selected single order. Based on the numerical calculation, we chose the -1 order, and then we surveyed the blaze angle, as shown in Fig. 10. We used the chief ray of the center field to evaluate the incidence angle to the grating. The combined FUV throughput from both dispersive optics is estimated to be $>30\%$.

While the selected diffractive orders are used to evaluate the as-designed Hyperion performance, in practice, all other diffraction orders are also present at their diffractive angles. These might combine and interfere with the required spectra, and this could harm the performance. For stray light mitigation in the design of the spectrometer, we deliberately positioned the optics and adjusted the incidence and diffractive angles so that the unwanted diffractive rays do not have a

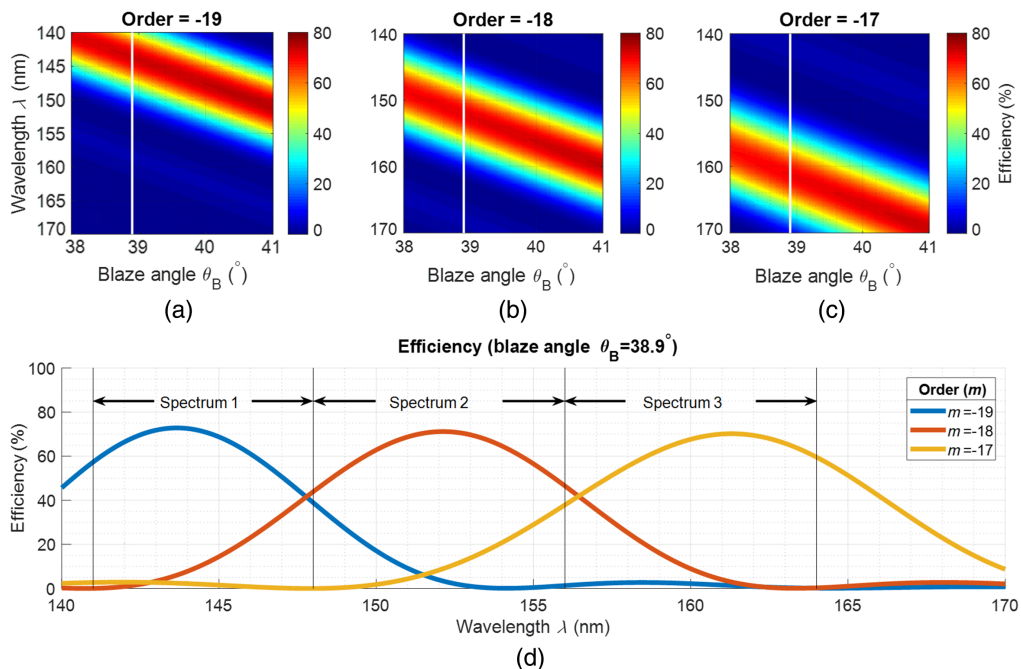


Fig. 9 The diffraction efficiency simulation of échelle grating.⁹ (a)–(c) The 2D efficiency plot for each diffraction order with blaze angle versus wavelength. Because the higher order was adapted, the $>40\%$ efficient range is 10 nm. We compromised the blaze angle to have even efficiency for all three spectrum stripes, and it was determined as 38.9 deg. The white line in the plot indicates the selected angle. (d) The overall efficiency of the full spectrum is presented. The spectrums 1 to 3 correspond to diffraction orders of -19 , -18 , and -17 , respectively. The chosen angle provides a fairly even efficiency trend, even though high orders are adopted for high spectral resolution.

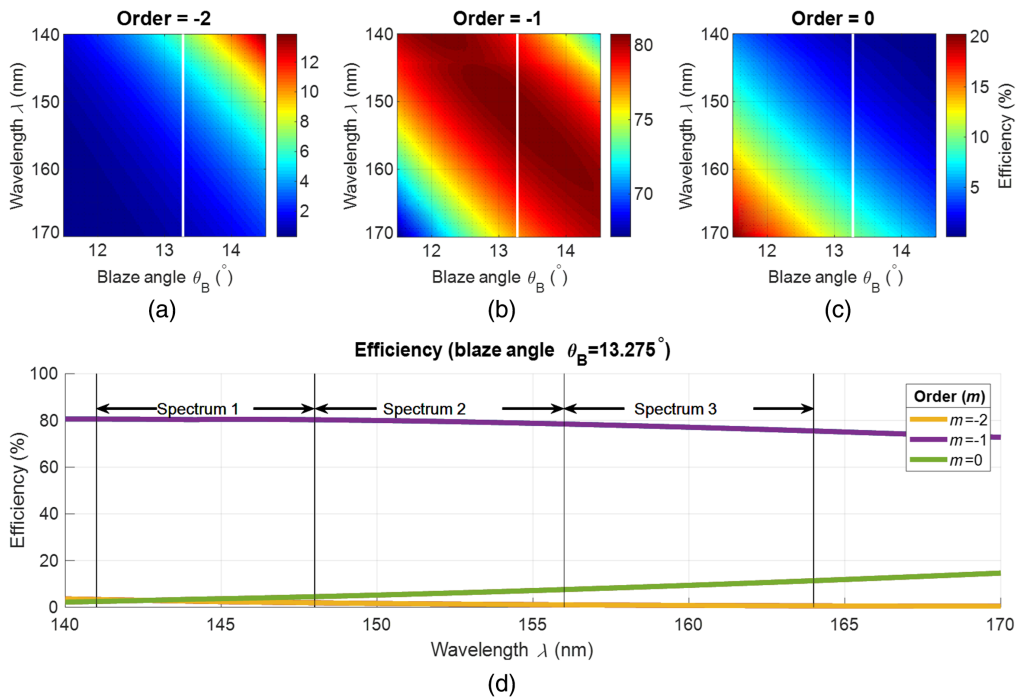


Fig. 10 The efficiency simulation of the second cross-dispersion grating. In contrast with the first échelle grating, the cross-dispersion grating uses a single order to separate overlapping bands in the orthogonal direction to the previous one. (a)–(c) The 2D efficiency plots of candidate orders. The -1 order is selected so that it has flat efficiency. (d) The selected order (-1) mitigates the cross-talk from the neighboring orders (-2 and 0) due to the low energy of the -2 and 0 orders.

direct path to the remaining optical components. The equipment in the spectrometer (e.g., mirror back surface and grating mount, spectrometer box, sensor package, etc.) may reflect the unwanted beam. With a full optomechanical design and structure model, conventional black coatings and/or baffle designs can be performed using a nonsequential ray-tracing analysis to reduce out-of-band light leakage.

The effective area of Hyperion can be calculated using various factors including the simulated diffraction efficiency of gratings, the known optical coating properties of the optics, and the detector efficiency. We assumed 84% reflectance of MgF_2 coating and 3% contamination loss for all optical surfaces. Also, the high detector efficiency helps to achieve a relatively large effective area of Hyperion. The combined theoretical FUV effective area of Hyperion is 82.2 cm^2 for the 141- to 164-nm band.

5 Conclusion

We designed a high spectral resolution space telescope for FUV astrophysical observations. The δ -doped CCDs, developed by JPL, can extend the measurable spectral range of Hyperion to 141 nm. The on-axis layout of the telescope apparatus to the first grating and in-plan design for dispersive optics allows for intuitive aberration control. The low aberration of the imaging system ensures a spectral resolution of $R > 30,000$ and a spatial resolution of 3 arcsec. The geometric optics design and spectral properties were implemented and evaluated, and the first version of the Hyperion FUV telescope design was found to thoroughly address the scientific requirements. Finally, considering the absence of publicly shared literature pertaining to space FUV cross-dispersion design, this detailed design study will be a community serving reference and benchmark for further upgrading of Hyperion or any other FUV telescope design. Hyperion was submitted to the SMEX 2019 AO and was not selected. The Hyperion team is planning to revise the mission for the 2021 MDEX call.

6 Appendix A: Zernike Coefficients of the Freeform Imaging Optics (M4 and M5)

The Hyperion freeform imaging optics (i.e., M4 and M5) in the type-4 layout are specified with standard Zernike polynomials (order up to the 50th term) as presented in Table 4.

Table 4 Zernike coefficients of M4 and M5.

Zernike order	M4	M5	Zernike order	M4	M5
Z1	0	0	Z26	8.4550E-04	6.0302E-03
Z2	0	0	Z27	-8.1407E-04	-7.8854E-03
Z3	0	0	Z28	7.6077E-04	4.4187E-03
Z4	0	0	Z29	-3.7118E-05	4.3416E-05
Z5	-8.4423E-02	-2.0151E-01	Z30	1.7160E-04	-2.0768E-04
Z6	1.6340E-01	4.7898E-01	Z31	-1.1270E-04	1.3269E-04
Z7	1.0297E-03	5.1554E-03	Z32	1.8209E-04	-2.7551E-04
Z8	9.2819E-03	1.0824E-02	Z33	-1.4986E-04	3.1133E-04
Z9	-3.7554E-03	3.1418E-04	Z34	1.8857E-04	-3.3013E-04
Z10	6.1298E-03	-1.2628E-03	Z35	-2.8156E-04	6.2432E-04
Z11	2.0059E-03	1.6598E-02	Z36	1.6411E-04	-4.2171E-04
Z12	3.0545E-03	2.2751E-02	Z37	5.4825E-05	6.5784E-04
Z13	-1.2831E-03	-9.1575E-03	Z38	7.8881E-05	8.9076E-04
Z14	2.7191E-03	1.8961E-02	Z39	-3.3885E-05	-3.8011E-04
Z15	-1.6289E-03	-1.6400E-02	Z40	9.6133E-05	7.9478E-04
Z16	1.1988E-03	-2.2016E-03	Z41	-6.8013E-05	-7.3797E-04
Z17	-2.5137E-04	3.7981E-04	Z42	9.0764E-05	5.9947E-04
Z18	1.2232E-03	-2.3865E-03	Z43	-9.1705E-05	-1.0544E-03
Z19	-7.0145E-04	1.1996E-03	Z44	1.1968E-04	3.2030E-04
Z20	1.1981E-03	-2.4149E-03	Z45	-2.2777E-04	-1.5570E-03
Z21	-9.3501E-04	2.4403E-03	Z46	1.1646E-06	2.2783E-05
Z22	5.5002E-04	5.0973E-03	Z47	1.3209E-06	2.5427E-06
Z23	-3.4156E-04	-2.8136E-03	Z48	2.5765E-06	1.5571E-05
Z24	7.9740E-04	6.9101E-03	Z49	1.5422E-06	1.4213E-06
Z25	-5.8592E-04	-5.4489E-03	Z50	5.6492E-06	1.3347E-05

Acknowledgments

The authors would like to thank the Technology Research Initiative Fund (TRIF) Optics/Imaging Program, through the Wyant College of Optical Sciences at the University of Arizona and the Friends of Tucson Optics (FoTO) Endowed Scholarships in Optical Sciences.

References

1. D. Decataldo et al., “Photoevaporation of jeans-unstable molecular clumps,” *Mon. Not. R. Astron. Soc.* **487**, 3377 (2019).
2. R. J. Gould and E. E. Salpeter, “The interstellar abundance of the hydrogen molecule. I. Basic processes,” *Astrophys. J.* **138**, 393 (1963).
3. M. R. Krumholz, “The big problems in star formation: the star formation rate, stellar clustering, and the initial mass function,” *Phys. Rep.* **539**, 49 (2014).
4. R. C. Kennicutt, Jr., “Star formation in galaxies along the Hubble sequence,” *Annu. Rev. Astron. Astrophys.* **36**, 189 (1998).
5. K. L. Adelberger and C. C. Steidel, “Multiwavelength observations of dusty star formation at low and high redshift,” *Astrophys. J.* **544**, 218 (2000).
6. M. E. Hoenk et al., “Growth of a delta-doped silicon layer by molecular beam epitaxy on a charge-coupled device for reflection-limited ultraviolet quantum efficiency,” *Appl. Phys. Lett.* **61**, 1084 (1992).
7. S. Nikzad et al., “Delta-doped electron-multiplied CCD with absolute quantum efficiency over 50% in the near to far ultraviolet range for single photon counting applications,” *Appl. Opt.* **51**, 365 (2012).
8. M. E. Hoenk et al., “Superlattice-doped silicon detectors: progress and prospects,” *Proc. SPIE* **9154**, 915413 (2014).
9. H. Choi et al., “Hyperion: far-UV cross dispersion spectroscopy design,” *Proc. SPIE* **11487**, 114870W (2020).
10. A. Boggess et al., “The IUE spacecraft and instrumentation,” *Nature* **275**, 372 (1978).
11. Y. Kondo, A. Boggess, and S. P. Maran, “Astrophysical contributions of the international ultraviolet explorer,” *Annu. Rev. Astron. Astrophys.* **27**, 397 (1989).
12. R. A. Kimble et al., “The on-orbit performance of the space telescope imaging spectrograph,” *Astrophys. J. Lett.* **492**, L83 (1998).
13. D. A. Content et al., “Development and testing of diffraction gratings for the space telescope imaging spectrograph,” *Proc. SPIE* **2807**, 267 (1996).
14. J. C. Green et al., “The cosmic origins spectrograph,” *Astrophys. J.* **744**, 60 (2012).
15. P. Morrissey, “A GALEX instrument overview and lessons learned,” *Proc. SPIE* **6266**, 62660Y (2006).
16. R. Grange et al., “GALEX UV Grism for slitless spectroscopy survey,” *Proc. SPIE* **10569**, 1056908 (2017).
17. T. K. Wyder et al., “The ultraviolet galaxy luminosity function in the local universe from GALEX data,” *Astrophys. J. Lett.* **619**, L15 (2005).
18. D. J. Sahnou et al., “Design and predicted performance of the far ultraviolet spectroscopic explorer,” *Proc. SPIE* **2807**, 2 (1996).
19. S. R. McCandliss, “Molecular hydrogen optical depth templates for FUSE data analysis,” *Publ. Astron. Soc. Pac.* **115**, 651 (2003).
20. M. Hurwitz and S. Bowyer, “A high resolution spectrometer for EUV/FUV wavelengths,” *Proc. SPIE* **0627**, 375 (1986).
21. T. Harada et al., “Design of a high-resolution extreme-ultraviolet imaging spectrometer with aberration-corrected concave gratings,” *Appl. Opt.* **37**, 6803 (1998).
22. J. C. Green, E. Wilkinson, and S. D. Friedman, “Design of the far ultraviolet spectroscopic explorer spectrograph,” *Proc. SPIE* **2283**, 12 (1994).
23. K. France et al., “The LUVOR ultraviolet multi-object spectrograph (LUMOS): instrument definition and design,” *Proc. SPIE* **10397**, 1039713 (2017).
24. O. H. W. Siegmund et al., “UV imaging detectors with high performance microchannel plates,” *Proc. SPIE* **11118**, 111180N (2019).
25. M. Koike, “1. Normal-incidence monochromators and spectrometers,” *Exp. Methods Phys. Sci.* **32**, 1–20 (1998).
26. S. S. Vogt et al., “HIRES: the high-resolution Échelle spectrometer on the Keck 10-m Telescope,” *Proc. SPIE* **2198**, 362 (1994).
27. I. Trumper et al., “Design form classification of two-mirror unobstructed freeform telescopes,” *Opt. Eng.* **59**, 025105 (2020).

28. A. Bauer, E. M. Schiesser, and J. P. Rolland, “Starting geometry creation and design method for freeform optics,” *Nat. Commun.* **9**, 1756 (2018).
29. J. C. Papa, J. M. Howard, and J. P. Rolland, “Three-mirror freeform imagers,” *Proc. SPIE* **10690**, 106901D (2018).
30. W. J. Smith, “Modern lens design” (2005).
31. R. R. Shannon, *The Art and Science of Optical Design*, Cambridge University Press, Cambridge (1997).

Heejoo Choi is a research scholar at the James C. Wyant College of Optical Science, University of Arizona and an optical scientist at the Large Binocular Telescope. His specialties cover optical design and metrology for academia and industrial system. He contributed to the design, modeling, and testing of the multiple space projects. And he has been serving as a guest editor for Photonics in the MDPI journal and a committee of Optical Manufacturing and Testing (SPIE).

Isaac Trumper is the CTO of ELE Optics founded in 2020 to build optical software tools for the community. He received his PhD in 2019 from the College of Optical Sciences focusing on deflectometry, optical metrology, and freeform optical design. He received his bachelor’s from the Institute of Optics in 2015 studying optical metrology and design.

Yi-Ting Feng received her MS degree from James C. Wyant College of Optical Sciences at the University of Arizona in 2020. She is now pursuing her PhD in the Institute of Optics at the University of Rochester. Her current research mainly focuses in the area of physical optics and optical design. She has worked on optical simulations of large telescopes with segmented mirrors and diffraction elements design for telescope systems.

Hyukmo Kang is a fifth-year PhD candidate at Wyant College of Optical Sciences, the University of Arizona, and an instructor of Practical Optical System Design workshop (POW). He worked on optical design of spectroscopy module for the Large Binocular Telescope and an objective lens for augmented reality system. His research interests are in the optical design and the deflectometry which could be applied to freeform surfaces fabrications.

Joel Berkson received his BS degree in optical sciences and engineering from James C. Wyant College of Optical Sciences and is now a second-year PhD student in optical sciences. He has experience with LiDAR, optical design, and optical metrology for a variety of applications. His current research interests are deflectometry, fringe projection, and optical design.

Haeun Chung is a postdoctoral researcher at the Department of Astronomy/Steward Observatory of the University of Arizona. He works on the various ground and space-based UV/Visible astronomical instrumentation projects, including Aspera, Hyperion, FIREBall-2, K-SPEC, and DOTIFS. He received his PhD in astronomy from Seoul National University in 2019.

Erika Hamden is an astronomer at the University of Arizona. She specializes in UV detectors and instruments, with a science focus on observing emission from diffuse hydrogen. She is the PI of Hyperion.

Dae Wook Kim is an assistant professor of optical sciences and astronomy at the University of Arizona. His research area covers precision optical engineering, optics fabrication, and freeform metrology including interferometry and deflectometry. He is the chair of the Optical Manufacturing and Testing (SPIE) and Optical Fabrication and Testing (OSA) conferences. He has served as an associate editor for the *Optics Express* journal. He is a senior member of OSA and an SPIE fellow.